Reactions of Water with Radical Cations of Guanine, 9-Methylguanine, 2'-Deoxyguanosine and Guanosine: Keto-Enol Isomerization, C8-Hydroxylation, and Effects of N9-Substitution

Journal:	*Physical Chemistry Chemical Physics*
Manuscript ID	CP-ART-08-2018-005453.R1
Article Type:	Paper
Date Submitted by the Author:	13-Oct-2018
Complete List of Authors:	Sun, Yan; Queens College of the City University of New York, Chemistry and Biochemistry; The Graduate Center of the City Univeristy of New York, Ph.D. Program in Chemistry Zhou, Wenjing; Queens College of the City University of New York, Chemistry and Biochemistry Moe, May; Queens College of the City University of New York, Chemistry and Biochemistry Liu, Jianbo; Queens College of the City University of New York, Chemistry and Biochemistry; The Graduate Center of the City Univeristy of New York, Ph.D. Program in Chemistry

Reactions of Water with Radical Cations of Guanine, 9-Methylguanine, 2′-Deoxyguanosine and Guanosine: Keto-Enol Isomerization, C8-Hydroxylation, and Effects of N9-Substitution

Yan Sun,[ab] Wenjing Zhou,[a] May Myat Moe,[a] and Jianbo Liu*[ab]

[a] Department of Chemistry and Biochemistry, Queens College of the City University of New York, 65-30 Kissena Blvd., Queens, NY 11367, USA

[b] Ph.D. Program in Chemistry, The Graduate Center of the City University of New York, 365 5th Ave., New York, NY 10016, USA

Abstract The reactions of D_2O with radical cations of guanine (9HG$^{\bullet+}$), 9-methylguanine (9MG$^{\bullet+}$), 2′-deoxyguanosine (dGuo$^{\bullet+}$) and guanosine (Guo$^{\bullet+}$) were studied in the gas phase, including measurements of reaction cross sections over a center-of-mass collision energy (E_{col}) range from 0.1 to 2.0 eV and computation of reaction pathways at DLPNO-CCSD(T)/aug-cc-pVTZ//ωB97XD/ 6-31+G(d,p). Reaction efficiencies of all radical cations are well below unity (~2% of collision rate), despite there being exoergic pathways. For each reactant ion, the energetically most favorable product channel corresponds to formation of water complexes; however, this channel accounts for only 5% of the total cross section at lowest E_{col} and becomes negligible at high E_{col} due to short complex lifetimes. The dominant product channel is H/D exchange that appears to be complex-mediated at low E_{col}, but switches to a direct mechanism and accompanies keto-enol isomerization of guanine moiety when E_{col} increases. C8-hydroxylation, a minor yet the most biologically important channel, was observed for 9HG$^{\bullet+}$; and its mechanism was elucidated in the presence of single and double water molecules, of which the second water eliminates the barrier for C8-addition via a proton shuttle mechanism. All reactions show strong dependence on radical structures, with overall reactivity being 9HG$^{\bullet+}$ >> 9MG$^{\bullet+}$ > dGuo$^{\bullet+}$ ≈ Guo$^{\bullet+}$. Reaction dynamics of 9HG$^{\bullet+}$ and 9MG$^{\bullet+}$ with water was simulated at E_{col} = 0.1 eV using ωB97XD/ 6-31+G(d), to reveal complex formation at the early stage of reactions and the effects of N9-substitution. Trajectory results suggest that the missing of a W9 complex (water bonded to N9-H) is responsible for the reduced reactivity of N9-substituted radical cations; but the relatively long-lived W16 complexes (water bonded to N1-H and C6-O) of dGuo$^{\bullet+}$ and Guo$^{\bullet+}$ may enhance keto-enol isomerization.

*Corresponding author. E-mail: jianbo.liu@qc.cuny.edu. Telephone: 1-718-997-3271.

I. Introduction

Among all DNA nucleobases, guanine (G) has the lowest oxidation potential ($E°$ vs. NHE = 1.29 V for guanosine, 1.10 – 1.24 V for the guanine moiety of DNA, 1.42 V for adenosine, 1.6 V for deoxycytidine, and 1.7 V for thymidine)[1, 2] and in parallel the lowest adiabatic ionization energy (AIE = 7.75 eV for G, 8.27 eV for adenine, 8.66 eV for cytosine, and 8.82 eV for thymine),[3, 4] and thus represents a preferential target for oxidation and ionization over adenine and pyrimidine bases. This leads to the formation of guanine radical cation $G^{\bullet+}$ in DNA upon radiolysis,[5, 6] mono-[7] and bi-photonic[8] UV laser photolysis, chemical oxidation,[9] electron transfer between metal complexes bound to DNA,[10] electrocatalytic oxidation,[11, 12] and type I photooxidation.[13, 14] Pairing guanine with cytosine in double-stranded (*ds*) DNA further decreases its oxidation potential,[15, 16] forcing radical cations (holes) initially formed on other nucleobases to migrate through duplex and eventually leading to the more stable $G^{\bullet+}$.[6, 17]

Scheme 1 outlines the intermediacy of $G^{\bullet+}$ in DNA post-ionization conversion.[18-23] An unique feature of $G^{\bullet+}$ is that it becomes more acidic, *i.e.* pK_a = 9.4 for guanosine and 3.9 for its radical cation.[5] As a consequence, $G^{\bullet+}$ loses its N1-proton[24] to water at neutral pH within 56 ns (rate constant $k = 1.8 \times 10^7$ s^{-1}).[25, 26] The resulting $[G - H]^{\bullet}$ does not directly react with water[27] and lives for 0.07 – 0.28 s in single-stranded (*ss*) DNA/oligonucleotide[28, 29] and 0.18 – 5 s in *ds* DNA/oligonucleotides,[29, 30] before its conversion to 2Ih,[22] Iz and Z[18] as depicted in Scheme 1. At low pH, the lifetime of $G^{\bullet+}$ is, in contrast, governed by C8-water addition to the formation of C8-hydroxylated guanine radical $[8\text{-OH-G} + H]^{\bullet+}$ — an intermediate that was proposed on the basis of the EPR/electron nuclear double resonance (ENDOR) measurement upon $OH^{\bullet}$ addition to a single crystal of N7-protonated guanine.[31] C8-hydroxylation completes within 3 ms ($k = 3.3 \times 10^2$ s^{-1} at pH 2.5),[28] followed by secondary oxidation to 8-oxo-7,8-dihydroguanine (OG, $k = 4 \times 10^9$ s^{-1}).[19, 20] OG is a widely used biomarker for oxidative stress within cells and tissues,[32, 33] and participates in a variety of biological sequelae including photocleavage,[34] G·C → A·T mutation,[35] Alzheimer′s[36] and Parkinson′s diseases,[37] and DNA–protein cross-linking.[38]

The aforedescribed $G^{\bullet+}$ kinetics indicates that free $G^{\bullet+}$ or that within *ss* DNA undergoes deprotonation

overwhelmingly at neutral pH[28] (5 orders of magnitude faster than hydration), and produces little OG.[39] This however does not represent the scenario within *ds* DNA, where the hydration of $G^{\bullet+}$ becomes more efficient[13] ($k = 6 \times 10^4$ s^{-1} at neutral pH[40]) as $G^{\bullet+}$ is stabilized through base stacking and base pairing which limit its ability to lose a proton, *i.e.*, the N1-proton (p*K*a 3.9)[5] of $G^{\bullet+}$ is shared with the N3 (p*K*a 4.3)[41] of cytosine, with an equilibrium constant K_{eq} estimated to be 2.5 for $G^{\bullet+}{\cdot}C \rightleftharpoons [G - H]^{\bullet}{\cdot}[C + H]^{+}$. Consequently, the formation of OG in *ds* DNA is a factor of 7 greater than in *ss* DNA.[29] These seeming contradictions imply that free $G^{\bullet+}$ in solution might not faithfully mimic the local environment experienced by nucleobases within DNA.[6] In this regard, gas-phase environment may be more appropriate for examining $G^{\bullet+}$ structure and reactivity, as deprotonation of $G^{\bullet+}$ shuts down in the gas phase and no longer competes with hydration.

$G^{\bullet+}$ was often generated by photolysis[5, 28, 42] or radiolysis[5, 24, 43] of $S_2O_8^{2-}$, Br^- or Cl^- solution where the resulting $SO_4^{\bullet-}$, $Br_2^{\bullet-}$ or $Cl_2^{\bullet-}$ in turn oxidized G to $G^{\bullet+}$, followed by measurements of radicals in solution or frozen/dry samples using transient absorption,[25, 28, 29, 42] IR,[14,44] resonance Raman, [43] and EPR.[24, 30, 31] The mechanistic aspects for formation and subsequent deprotonation of $G^{\bullet+}$ in the presence of $SO_4^{\bullet-}$ have been examined in G-quadruplexes by recent experimental[45] and theoretical[46] work. Gas-phase $G^{\bullet+}$ could be formed by electron-impact ionization (EI) of guanine[47] or fast atom bombardment (FAB) of a mixture of guanosine and dimethyloxynaphthalene in *m*-nitrobenzyl alcohol.[48] But EI and FAB generated substantial electronical and vibrational excitation and fragmentation of resulting radical ions. A pioneering work by Siu and co-workers[49] has shown that radical cations of tyrosyl-containing oligopeptides could be formed in the gas phase by collision-induced dissociation (CID) of $[Cu^{II}(\text{diethylenetriamine})(\text{oligopeptide})]^{\bullet 2+}$ that was formed in solution and electrosprayed into the gas phase. Later, O′Hair and McFadyen *et al.* produced radical cations of nucleobases in a similar procedure using Cu^{II} ternary complexes of terpyridine and nucleobases/nucleosides.[50, 51] Recently, Cheng and Bohme[52] and O′Hair and Orbell *et al*.[53] reported a more convenient way of producing nucleobase radical cations by CID of Cu^{II}-nucleoside binary complexes.

The successful generation of stable $G^{\bullet+}$ in the gas phase has made it possible to examine $G^{\bullet+}$ intrinsic reactivity unperturbed by solvent and counter ions. In the present work, reactions of water with radical cations of unsubstituted guanine ($9HG^{\bullet+}$, in a N9-H tautomeric form), 9-methylguanine ($9MG^{\bullet+}$), 2′-deoxyguanosine ($dGuo^{\bullet+}$) and guanosine ($Guo^{\bullet+}$) have been examined in the gas phase. We used tandem mass spectrometry coupled with ion-beam scattering to measure reaction cross sections, product branching ratios and their collision energy (E_{col}) dependence. The sensitivity of gas-phase experiment, corroborated with reaction potential energy surface (PES) calculations and dynamics simulations, has led to a better understanding of guanine radical ion chemistry.

II. Experimental and computational details

1. Ion-molecule scattering

Reactions were carried out on a home-made electrospray ionization (ESI) guided-ion-beam tandem mass spectrometer described in detail elsewhere.[54] The apparatus consists of an ESI ion-source, a radio frequency (rf) hexapole ion guide, a quadrupole mass filter, an rf octopole ion guide surrounded by a scattering cell, a second quadrupole mass filter, and a pulse-counting electron multiplier detector. Both quadrupoles use Extrel 9.5 mm diameter tri-filter rods operating at 2.1 MHz to cover a mass/charge (m/z) range of 1 – 500.

Right before the experiment, a sample solution was prepared in methanol/water (3:1 vol.) containing 0.25 mM $Cu(NO_3)_2$ (AlfaAesar, >99.999%) and 0.5 mM guanosine (Acros, 99%). The solution was sprayed into the ambient atmosphere through an electrospray needle at a flow rate of 0.06 mL/h, with the ESI potential of 2.35 kV relative to ground. Positively charged droplets entered the source chamber of the mass spectrometer through a pressure-reducing desolvation capillary. The distance between the emission tip of the ESI needle and the sampling orifice of the capillary was 7 mm. The capillary was biased at 115 V and heated to a temperature tuned between 180 and 200 ºC to maximize desired ion intensities. Liquid aerosols underwent desolvation as they passed through the capillary, converting to a mixture of gas-phase doubly charged $[Cu^{II}(Guo)_{0\text{-}6}(MeOH)_{0\text{-}3}]^{\bullet 2+}$.[52, 53] Ions were focused toward the

capillary axis by gas flow and then transported into the source chamber that was evacuated to a pressure of 1.7 Torr. A skimmer with an orifice of 1.5 mm is located 3 mm away from the capillary end, separating the source chamber and the hexapole ion guide. The skimmer was biased at 17 – 25 V relative to ground. The electrical field between the capillary and the skimmer prompted CID of $[Cu^{II}(Guo)_{0-6}(MeOH)_{0-3}]^{\bullet 2+}$ with background gas within the chamber, of which the fragmentation of $[Cu^{II}(Guo)_3]^{\bullet 2+}$ and $[Cu^{II}(Guo)(MeOH)_2]^{\bullet 2+}$ is featured by production of $Guo^{\bullet +}$ via redox charge separation followed by dissociation due to Coulombic repulsion within the complex, and the resulting $Guo^{\bullet +}$ may rupture the N-glycosidic bond and produce $9HG^{\bullet +}$, *i.e.* eqs. (1 – 3): [52, 53]

$$[Cu^{II}(Guo)_3]^{\bullet 2+} \rightarrow [Cu(Guo)_2]^{+} + Guo^{\bullet +} \quad (1)$$

$$[Cu^{II}(Guo)(MeOH)_2]^{\bullet 2+} \rightarrow [Cu(MeOH)_2]^{+} + Guo^{\bullet +} \quad (2)$$

$$Guo^{\bullet +} \rightarrow 9HG^{\bullet +} + C_5H_8O_4 \quad (3)$$

$9MG^{\bullet +}$ and $dGuo^{\bullet +}$ were generated via in-source CID of $[Cu^{II}(9MG)_3]^{\bullet 2+}$ and $[Cu^{II}(dGuo)_3]^{\bullet 2+}$, for which the ESI solution was prepared using a mixing of 0.25 mM $Cu(NO_3)_2$ and 0.5 mM 9MG (Aldrich, ≥ 98.0%) or dGuo (Sigma, > 99%).

Radical cations that emerged from the skimmer were transported into the hexapole ion guide at a pressure of 24 mTorr, undergoing collisional focusing and thermalization to ~310 K. Radical cations subsequently passed into the first quadrupole mass filter for selection of specific radical ions. Mass-selected radical ions were collected and collimated by a lens set. The combination of collisional damping within the hexapole and the controlled collection radius at the quadrupole exit produced a mass-selected ion beam with narrow kinetic energy spread. Mass-selected reactant ions were injected into the octopole ion guide, which trapped ions in the radial direction. The octopole is surrounded by the scattering cell. D_2O (Magnisolv, 99.9%) was held in a thermostated glass reservoir, purified by freeze-pump-thaw cycles before the experiment, and leaked into the scattering cell through a leak valve. The valve was kept at 80°C to avoid freezing D_2O in the valve orifice. The scattering cell pressure was controlled at less than 0.08 mTorr (unless otherwise stated) and measured by a capacitance manometer

(MKS 690 head and 670 signal conditioner). Under these conditions, reactant radical cations underwent at most a single collision with D_2O. A DC bias voltage was applied to the octopole, allowing the control of the kinetic energy of reactant ions in the laboratory frame (E_{Lab}) and thus the E_{col} between reactant ions and D_2O molecules in the center-of-mass frame using $E_{col} = E_{Lab} \times m_{\text{neutral}}/(m_{\text{ion}} + m_{\text{neutral}})$, where m_{neutral} and m_{ion} are the masses of neutral and ionic reactants, respectively. After passing through the scattering cell, remaining reactant ions and product ions drifted to the end of the octopole, and then were *m/z* analyzed by the second quadrupole and counted by the electron multiplier.

Intensities of reactant ion beam were $3 - 5 \times 10^5$ counts/s for $9HG^{\bullet+}$ and $9MG^{\bullet+}$, and $1.2 - 1.5 \times 10^5$ counts/s for $dGuo^{\bullet+}$ and $Guo^{\bullet+}$. Initial kinetic energy of the ion beam was set to 0.9 eV with an energy spread of 0.6 eV that corresponds to an E_{col} resolution better than 0.07 eV. Reaction cross sections were calculated from the ratios of reactant and product ion intensities, the D_2O pressure in the scattering cell, and the effective cell length. Experiment was repeated multiple times and cycled through different E_{col} each time. Based on the reproducibility of measurements, the relative error of reaction cross sections (*e.g.* uncertainty in comparing data at different E_{col}) was estimated to be ≤ 20%.

2. Electronic structure calculations

Density functional theory (DFT) has been extensively used for calculating the structures and reactions of nucleobase and nucleoside radical cations in the gas phase[3, 15, 16, 27, 53, 55-58] and in solution.[15, 16, 56, 57, 59] Compared to B3LYP that suffers from spin-contamination for doublet systems[27] and self-interaction errors (SIE), ωB97XD[60] mitigates SIE and improves orbital descriptions of ionized states.[58] Therefore, reactants, intermediates, transition states (TSs) and products were calculated using ωB97XD paired with the 6-31+G(d,p) basis set. Conformation search was conducted for reactant ions, and their lowest-energy conformers were used as starting structures in PESs and dynamics simulations. TSs were verified as first-order saddle points, and the vibrational mode associated with an imaginary frequency corresponds to the anticipated reaction pathway. Aside from local criterion, intrinsic reaction coordinate (IRC) calculations were carried out to verify reactant/product minima connected through the TSs.

The ωB97XD-predicted stability order of conformers was affirmed by MP2/6-31+G(d,p). To benchmark the accuracy of ωB97XD/6-31+G(d,p) energies, we calculated AIEs for 9HG and 9MG and gas-phase acidities (GA) for $9MG^{\bullet+}$. ωB97XD/6-31+G(d,p)-calculated AIEs are 7.69 eV for 9HG and 7.53 eV for 9MG. For comparison, other predications are 7.65 – 7.68 eV (9HG) and 7.49 eV (9MG) at B3LYP/6-31++G(d,p),[3, 15, 16] 7.71 eV (9HG) and 7.53 eV (9MG) at ωB97XD/6-31++G(d), 7.79 eV (9HG) and 7.64 eV (9MG) at M06-2X/6-31++G(d),[58] 7.82 eV (9HG) at MP2/6-311++G(d,p),[61] 7.65 eV (9HG) at CASPT2(IPEA=0.25) //CASSCF/ANO-L 431/21,[62] and 7.89 eV (9HG) at G3MP2B3-ROMP2;[63] and the VUV photoionization-measured AIE is 7.75 eV for 9HG.[3] The ωB97XD/6-31+G(d,p)-calculated GA of $9MG^{\bullet+}$ is 967.8 kJ/mol. The value was refined to 950.8 kJ/mol by single-point calculation at DLPNO-CCSD(T)/aug-cc-pVTZ (the domain based local pair-natural orbital coupled-cluster method with single-, double- and perturbative triple excitations[64]) using ωB97XD optimized geometries. The latter value is in an excellent agreement with the experimental value of 952 ± 10 kJ/mol measured using Cooks′ kinetic method.[65] Encouraged by the improved accuracy of this combination method, reaction enthalpies ($\Delta_r H°$ at 298 K, with respect to reactants) were determined on the basis of electronic energies calculated at DLPNO-CCSD(T)/aug-cc-pVTZ//ωB97XD/6-31+G(d,p) and thermal corrections calculated at ωB97XD/6-31+G(d,p). The ωB97XD vibrational frequencies and zero-point energies (ZPEs) were scaled by a factor of 0.95 and 0.974,[66] respectively. DFT and MP2 calculations were carried out using Gaussian 09,[67] and DLPNO-CCSD(T) calculations and T1 diagnostic were accomplished using ORCA 3.0.3.[68] Complex lifetimes were analyzed on the basis of Rice-Ramsperger-Kassel-Marcus (RRKM) theory,[69] for which unimolecular rate constants were calculated using the program of Zhu and Hase.[70]

3. Direct dynamics trajectory simulations

Collision dynamics of $9HG^{\bullet+}$ and $9MG^{\bullet+}$ with water was simulated at E_{col} = 0.1 eV, using the Venus software[71, 72] to set up trajectory initial conditions, and the Hessian-based predictor-corrector algorithm[73] implemented in Gaussian 09 to integrate the classical equations of motion, with Hessian matrix updated every five steps. The initial separation between the centers of mass of randomly oriented collision

partners was set at 8.0 Å (where the attractive potential between reactants is negligible), with a collision impact parameter of 0 Å. The vibrational and rotational temperatures of reactants were set at 300 K to mimic the ion-molecule experiment. Quasi-classical Boltzmann sampling[74] was used to select vibrational and rotational energies. A quadratically convergent SCF method was used in case the conventional first-order SCF algorithm failed to converge. Trajectories were terminated when the product separation exceeded 8.8 Å or the maximum trajectory integration time (5000 fs) was reached.

ωB97XD/6-31+G(d) was used for the simulations as it provided the similar calculation accuracy as ωB97XD/6-31+G(d,p) but at a less computational cost. 100 trajectories were accomplished for each of $9HG^{\bullet+} + H_2O$ and $9MG^{\bullet+} + H_2O$. Trajectories of $9HG^{\bullet+}$ each took ~ 4300 CPU hours on an Intel 2.6 GHz core-based computational cluster, while those of $9MG^{\bullet+}$ each took ~ 6100 CPU hours. Trajectories of representative collisions were recalculated at ωB97XD/6-31+G(d,p) to test how a basis set with the explicit polarization term for H affects trajectory outcomes. The ωB97XD/6-31+G(d,p) trajectories reproduced the collision dynamics observed at ωB97XD/6-31+G(d), and the difference between the two sets of trajectories is within statistical uncertainty. gOpenMol[75] was used for trajectory visualization. Individual trajectories and ensemble averages were analyzed using programs written for these purposes.

III. Results

1. Structures of radical cations

We have examined all low-lying structures of $9HG^{\bullet+}$, $9MG^{\bullet+}$, $dGuo^{\bullet+}$ and $Guo^{\bullet+}$, taking into account the N9H–N7H tautomerization of guanine and the *anti*- and *syn*-conformations about the N-glycosidic bond of $dGuo^{\bullet+}$ and $Guo^{\bullet+}$. Their structures (Figs. S1 – S4) and Cartesian coordinates are provided in the Supporting Information. All structures have no spin contamination ($<S^2> = 0.750$, as expected for a radical), and the T1 values from CCSD(T) calculations did not exceed the upper limit of 0.02 (above which non-dynamic correlation effects are large enough to make single-reference method unreliable).[76]

Guanine has N9-H and N7-H tautomers, of which $7HG^{\bullet+}$ lies in energy at least 0.11 eV above $9HG^{\bullet+}$ and thus is unimportant. The global minima of $9HG^{\bullet+}$, $9MG^{\bullet+}$, $dGuo^{\bullet+}$ and $Guo^{\bullet+}$ all adopt a keto-

conformation for the guanine moiety. The sugar groups of dGuo$^{\bullet+}$ and Guo$^{\bullet+}$ prefer an *anti*-keto configuration, opposite to the *syn*-enol conformation found for gas-phase neutral dGuo[77] and Guo.[78] The calculated lowest-energy structures are consistent with IR spectra and CID of gas-phase 9MG$^{\bullet+}$[65] and dGuo$^{\bullet+}$.[53, 55] On the basis of their populations at 298 K, these lowest-energy conformers should be overwhelmingly dominating in our experiment and were thus used in the discussion of reactions.

To demonstrate the location of the unpaired electron, spin density contours for the lowest-energy 9HG$^{\bullet+}$, 9MG$^{\bullet+}$, dGuo$^{\bullet+}$ and Guo$^{\bullet+}$ are plotted in Fig. 1, along with charge distributions. For comparison, both keto and enol conformers are included in the figure. All radical cations share the same spin density distribution in that an unpaired electron is delocalized among N3, C5 and C8. Charge is separated from spin and C8-H is more positively charged than other groups, making this site vulnerable for nucleophilic water attack. An obvious consequence of the substitution of N9-H is reflected on charge densities, *i.e.*, the negative charge on N9 decreases from -0.38 at 9HG$^{\bullet+}$ to -0.11 at 9MG$^{\bullet+}$, -0.06 at dGuo$^{\bullet+}$ and -0.04 Guo$^{\bullet+}$; meanwhile the charge on C4 changes from +0.10 at 9HG$^{\bullet+}$ to -0.07 at 9MG$^{\bullet+}$, -0.25 at dGuo$^{\bullet+}$ and -0.26 at Guo$^{\bullet+}$. Charges on C6 and C8 also changes at dGuo$^{\bullet+}$ and Guo$^{\bullet+}$. We tend to attribute these changes to hyperconjugation and the associated electron delocalization between the π bonds of guanine and the σ bond of the substituent. When the dihedral angle of C4-N9-C1′-O(sugar) is distorted from the original -121° to 0° so that the σ(C1′-O) bond lies perpendicular to the π orbitals, changes of the charge distributions become less substantial.

2. Reaction products, enthalpies and cross sections

The radical cations + D_2O isotope combination was used in the experiment to look for possible atom scrambling. For all of the four reactant ions, major product channels include formation of water complexes (*i.e.* hydration), H/D exchange (H/D_Ex) and water-assisted keto-enol isomerization, as shown in reactions (4) – (7) where the presence of deuterium is indicated. H/D exchange and keto-enol isomerization have the same product ion mass. For the reaction of 9HG$^{\bullet+}$, product ions were observed for H elimination (HE), *i.e.* reaction (4d). Reaction enthalpies $\Delta_r H°$(298 K) were obtained from

DLPNO-CCSD(T)/aug-cc-pVTZ//ωB97XD/6-31+G(d,p) calculations, and those for H/D exchange were calculated from ZPE changes with deuteration occurring at different H positions.

$9HG^{\bullet+}$(*m/z* 151) + $D_2O \rightarrow$	$9HG^{\bullet+}\cdot D_2O$ (*m/z* 171)	hydration	$\Delta_rH°$ = -0.50 – -0.70 eV	(4a)
	d_1-$9HG^{\bullet+}$ (*m/z* 152) + HDO	H/D_Ex	$\Delta_rH°$ = -0.007 – -0.01 eV	(4b)
	d_1-enol-$9HG^{\bullet+}$ (*m/z* 152) + HDO	keto-enol	$\Delta_rH°$ = 0.06 eV	(4c)
	8-OD-G^+ (*m/z* 170) + H	HE	$\Delta_rH°$ = 0.99 eV	(4d)
$9MG^{\bullet+}$ (*m/z* 165) + $D_2O \rightarrow$	$9MG^{\bullet+}\cdot D_2O$ (*m/z* 185)		$\Delta_rH°$ = -0.37 – -0.68 eV	(5a)
	d_1-$9MG^{\bullet+}$ (*m/z* 166) + HDO		$\Delta_rH°$ = -0.006 – -0.009 eV	(5b)
	d_1-enol-$9MG^{\bullet+}$ (*m/z* 166) + HDO		$\Delta_rH°$ = 0.06 eV	(5c)
$dGuo^{\bullet+}$(*m/z* 267) + $D_2O \rightarrow$	$dGuo^{\bullet+}\cdot D_2O$ (*m/z* 287)		$\Delta_rH°$ = -0.29 – -0.65 eV	(6a)
	d_1-$dGuo^{\bullet+}$ (*m/z* 268) + HDO		$\Delta_rH°$ = -0.006 – -0.007 eV	(6b)
	d_1-enol-$dGuo^{\bullet+}$ (*m/z* 268) + HDO		$\Delta_rH°$ = 0.07 eV	(6c)
$Guo^{\bullet+}$(*m/z* 283) + $D_2O \rightarrow$	$Guo^{\bullet+}\cdot D_2O$ (*m/z* 303)		$\Delta_rH°$ = -0.26 – -0.64 eV	(7a)
	d_1-$Guo^{\bullet+}$ (*m/z* 284) + HDO		$\Delta_rH°$ = -0.006 – -0.008 eV	(7b)
	d_1-enol-$Guo^{\bullet+}$ (*m/z* 284) + HDO		$\Delta_rH°$ = 0.07 eV	(7c)

In the experiment, all hydration products were formed under single hit conditions where reactant ion reacts with water once or not at all, therefore the geometries of mono-hydrated products were predicted by adding a water molecule to all possible hydration sites[79] of reactant radical cations and then optimized at ωB97XD/6-31+G(d,p). The optimized hydration structures are summarized in Fig. 2, of which the hydration sites are specified in notations. The range of $\Delta_rH°$ listed for hydration reactions indicates the formation of all possible hydration structures, including W12a (*i.e.* water hydrogen-bonded to N1-H and N2-H2a), W16, W9 and W2b for $9HG^{\bullet+}\cdot H_2O$, and W12a, W16, W2b and W8 (or W85′) for $9MG^{\bullet+}\cdot H_2O$, $dGuo^{\bullet+}\cdot H_2O$ and $Guo^{\bullet+}\cdot H_2O$. $dGuo^{\bullet+}\cdot H_2O$ and $Guo^{\bullet+}\cdot H_2O$ have additional sugar-hydrated structures. It was found that the water ligand has no obvious influence on spin and charge densities of the radical cations. Attempt was made to optimize complex structures where water is hydrogen-bonded to the lone-pair electron at N3 or N7, but none of these structures converged to stable complexes. Neither

were such structures found in direct dynamics simulations (*vide infra*).

Reaction cross sections for individual product channels are shown in Fig. 3. Error bars were estimated by the variations between multiple experimental data sets. Reactions at E_{col} less than 0.1 eV produced very slow product ions that could not be collected efficiently due to potential barriers in the ion guide. Therefore, reaction cross sections were reported over a center-of-mass E_{col} range from 0.1 to 2.0 eV. To increase HE product ion intensity, a relatively high D_2O pressure (~ 0.2 mTorr) was used in the scattering cell; as a result, both single- (~20%) and multiple- (~8%) collisions have contributed to the measured HE cross section. Fig. 3c only shows HE for $9HG^{\bullet+} + D_2O$, as the cross sections for the other three reaction systems are too small to measure E_{col} dependence. What could be confirmed qualitatively is that all systems had H elimination at lowest E_{col}, which should be mostly attributed to multiple collisions. The total reaction efficiency can be calculated as the ratio of $\sigma_{\text{total}}/\sigma_{\text{capture}}$, where σ_{capture} is the ion-neutral dipole capture cross section determined using the statistical adiabatic channel model.[80] The efficiencies at lowest E_{col} are 2% for $9HG^{\bullet+}$, 0.45% for $9MG^{\bullet+}$, 0.15% for $dGuo^{\bullet+}$ and 0.1% for $Guo^{\bullet+}$.

No proton transfer reaction of $G^{\bullet+} + D_2O \rightarrow [G - H]^{\bullet} + HD_2O^{+}$ was seem at E_{col} up to 2.0 eV, since the reaction was calculated to be endothermic by 2.81, 2.64, 2.86 or 2.73 eV when the proton is abstracted from guanine N1, N2a, N2b and N9, respectively. Neither did we observe the hydrogen abstract reaction of $G^{\bullet+} + D_2O \rightarrow [G + D]^{+} + OD^{\bullet}$, as the reaction is 1.70 eV endothermic and thus disfavored in the present E_{col} range.

3. Trajectory results

For a complex system, use of chemical intuition to predict reaction pathways may prove unreliable as there exist multiple concurrent and competing processes. Therefore, direct dynamics trajectories were calculated for $9HG^{\bullet+} + H_2O$ and $9MG^{\bullet+} + H_2O$ at E_{col} = 0.1 eV (100 trajectories for each). Dynamics simulations explore multiple minima in the conformation landscape and the reaction PES. The motion of molecules is followed, allowing the molecules to show what the preferred reaction pathways are.[73, 81-84] Of the 200 trajectories we have simulated, 31.5% can be characterized as direct, nonreactive scattering,

resulting in conversion of some E_{col} into vibrational and rotational energies. The remaining trajectories first form electrostatic complexes upon collisions. Such collision complexes do not have well-defined geometries or directional hydrogen bonds. They are simply floppy complexes of reactants, with large-amplitude intermolecular motion. The importance of these complexes, referred to as precursors in the remainder of discussion, is that they allow repeated encounters between reactants, increasing the probability of eventually locking into a stable hydrogen bond such as W12a. Still, a large fraction of precursors dissociate to reactants before the end of trajectories.

Two representative trajectories of forming $9MG^{\bullet+}{\cdot}H_2O$ are illustrated in Fig. 4a and b, where each frame shows collision time scale, changes in system potential energy (PE) and the centers-of-mass distance between collision partners, and changes of hydrogen bonds along the trajectory. In the trajectory of Fig 4a, the collision instant is around 300 fs, after that a precursor forms and then converges to a W12a structure at 1000 fs as shown by the formation of rH1–water and rH2a–water hydrogen bonds in the bottom frame. The two gray levels within the bottom frame mark the maximum distances for weak and modest interactions, respectively. The oscillations in the PE and bond lengths reflect molecular vibrations (including ZPE) and intermolecular motions. The trajectory in Fig. 4b represents the formation of a W8 complex. Note that W8 forms only in the trajectories of $9MG^{\bullet+} + H_2O$, and the nature of W8 is more electrostatic attraction than a hydrogen bond.

Our trajectory simulation times (~5 ps) were too short compared to the ion time-of-flight within the mass spectrometer, therefore we could not predict the distribution of complex structures in final product ions as most of the complexes would eventually dissociate driven by the acquired hydration enthalpy, and some trajectories may interconvert between different hydrogen bonds. The purpose of our dynamics simulations was to examine reaction dynamics at the early stage — the point at the reaction coordinate where different product channels and the effects of reactant structure originate. To this end, formation probabilities of different complex structures in the trajectories of $9HG^{\bullet+} + H_2O$ and $9MG^{\bullet+} + H_2O$ are compared in the histograms of Fig. 4c. The overall height of each column represents the total formation

probability of individual structures, and the white area represents the fraction of complexes that dissociate to starting reactants before the end of trajectories.

W12a was observed in both $9HG^{\bullet+} + H_2O$ and $9MG^{\bullet+} + H_2O$ trajectories, as the most probable structure in complex forming. W12a also has the strongest hydrogen bond among all hydration structures, according to DFT calculations in Fig. 2. Surprisingly, the yield of W16 is minor in both $9HG^{\bullet+}$ and $9MG^{\bullet+}$ trajectories, despite it represents the second strongest hydrogen bond. In sharp contrast, W8 diminishes in the trajectories of $9HG^{\bullet+} + H_2O$, whereas W9 diminishes in $9MG^{\bullet+} + H_2O$. As mentioned above W8 is more an electrostatic complex than hydrogen-bonded. We tried to optimize a W8-like structure for $9HG^{\bullet+}\cdot H_2O$, but the water always swings out of the original position and directs to a W9 structure. To compensate the missing of the W9 structure, $9MG^{\bullet+} + H_2O$ forms much more W2b and precursor than $9HG^{\bullet+} + H_2O$. The overall complex formation efficiencies are 69% for $9HG^{\bullet+} + H_2O$ and 68% for $9MG^{\bullet+} + H_2O$; but $9MG^{\bullet+} + H_2O$ produces more precursors (40%) than $9HG^{\bullet+} + H_2O$ (32%), and consequently presents a higher dissociation rate, *i.e.*, 35% of $9MG^{\bullet+}\cdot H_2O$ dissociate before the end of trajectories, and the rate drops to 30% for $9HG^{\bullet+}\cdot H_2O$.

IV. Discussion

1. Hydration complexes, H/D exchange and keto-enol isomerization

Despite the fact that formation of water complexes is the energetically most favorable, water complexes were detected only at low E_{col} and even then $\sigma_{\text{Hydration}}$ is at most 5% of the total cross section. We have calculated the lifetimes of various water complexes using the RRKM theory. For decay of these complexes to reactants, orbiting transition states[85] were assumed because there are no reverse barriers. In the calculations, we used average angular momenta corresponding to capture cross sections, *i. e.* $L = \mu \cdot v_{\text{rel}} \cdot (\sigma_{\text{capture}}/\pi)^{1/2}$ where μ and v_{rel} are the reduced mass and relative velocity of collision partners, respectively. Recoil energy needed to calculate orbiting TSs was estimated from dynamics trajectories. The average lifetime of $9HG^{\bullet+}\cdot H_2O$ is 70 – 80 ns at E_{col} = 0.1 eV, dropping to 3 ns at 0.2 eV and 0.1 ns at 0.5 eV. $9MG^{\bullet+}\cdot H_2O$ is longer lived than $9HG^{\bullet+}\cdot H_2O$, with an average lifetime of 1 μs at E_{col} = 0.1 eV,

60 ns at 0.2 eV and 2 ns at 0.5 eV. The longest lived complexes correspond to $dGuo^{\bullet+}\cdot H_2O$ and $Guo^{\bullet+}\cdot H_2O$. Their lifetimes are > 10 μs at E_{col} = 0.1 eV, 0.5 μs at 0.2 eV and 3 ns at 0.5 eV. The RRKM results imply that the lifetimes of all water complexes are shorter compared to ion time-of-flight (μs) in the mass spectrometer, and most complexes decayed back to reactants before reaching the ion detector. The mass spectrometer collected only a very small fraction of hydration products.

The dominant product channel for all reactant ions is H/D exchange. Note that keto-enol isomerization could only be observed in the experiment if there was concomitant H/D exchange. An obvious question is the extent to which simple H/D scrambling (without structure rearrangement) and keto-enol isomerization each contribute to the product cross section, and how their contributions vary with E_{col}. Our experiment could not distinguish which guanine tautomer formed in the products, but has provided clues through the reaction E_{col}-dependence. At low energies H/D exchange is strongly suppressed by E_{col}, and its cross section approaches a minimum at E_{col} = 0.2 – 0.4 eV. However, the cross section rebounds starting from 0.3 eV, becoming energy-independent toward high E_{col} limit. Such E_{col} dependence suggests that H/D exchange is dominated by one mechanism at lowest E_{col}, while a second mechanism grows at high E_{col}. The low-energy H/D exchange is most likely mediated by a complex and proceeds via hydrogen migration or isomerization of hydrogen bonds, with the formation probability and/or lifetime of such migrated complexes strongly suppressed by E_{col}. A complex-mediated H/D exchange at low E_{col} is consistent with the same dependence of complex-forming and H/D exchange cross sections on reactant ion structures (see Fig. 3a and b). The endothermic keto-enol isomerization may contribute to low energy reactions, but cannot be dominant as judged from the E_{col}-inhibiting feature of the reaction. The high-energy mechanism, on the other hand, can be mostly attributed to water-assisted keto-enol isomerization. The PES for reaction (4c) is depicted in Fig. 5. There are many complexes form in collisions, but reaction (4c) must certainly pass through W16. The TS for isomerization can be characterized as double proton transfers occurring simultaneously, with activation barrier 0.53 eV above $9HG^{\bullet+}\cdot$W16, but still 0.07 eV below reactants. Catalyzed by water, the

reaction has a threshold of only 0.06 eV. Keto-enol isomerization may also be possible for dry radical cations via a direct N1-to-O6 proton transfer. We have calculated TS(no water) in Fig. 5 for the direct version of keto-enol isomerization. The barrier rises to 1.69 eV above starting reactants, rendering the isomerization of dry guanine less likely. Similar water-assisted isomerization was observed for neutral 8-hydroxyl guanine radical.[86]

The above discussion leads to a dynamics picture as follows: 1) at low energies, a set of short-lived water complexes form, and before dying out a fraction of them mediate H/D exchange; 2) as E_{col} raises, the probability of complex forming decreases rapidly. It is more reasonable to assume that keto-enol isomerization occurs in an already correctly oriented (W16-like) structure allowing for double proton transfer, by which we mean that reactivity is controlled by collision geometry; 3) As an additional note, $dGuo^{\bullet+}\cdot H_2O$ and $Guo^{\bullet+}\cdot H_2O$ can carry the water ligand longer than $9HG^{\bullet+}\cdot H_2O$ and $9MG^{\bullet+}\cdot H_2O$ at high E_{col} (a phenomena that could be rationalized in terms of increased degrees of freedom and more efficient IVR in large systems), of which the W16 structure could catalyze keto-enol isomerization. This is supported by the experimental observation that H/D exchange for $dGuo^{\bullet+}$ and $Guo^{\bullet+}$ does not undergo steep decreasing as $9HG^{\bullet+}$ and $9MG^{\bullet+}$ when E_{col} starts increasing, and have higher σ_{H/D_EX} than $9HG^{\bullet+}$ and $9MG^{\bullet+}$ at high energies. Of course, a direct mechanism still dominates for $dGuo^{\bullet+}$ and $Guo^{\bullet+}$ at high energies.

2. C8-hydroxylation and H elimination

Perhaps the biologically most relevant product channel is the water attack at the C8 position of guanine radical cations, as this is the first step toward the cascade of the OG lesions. Despite the pivotal role, the C8-adduct $[8\text{-OH-G} + H]^{\bullet+}$ has never been directly detected except EPR/ENDOR measurement of $OH^{\bullet}$ addition to solid N7-protonated guanine.[31] Schuster and co-worker[87] reported an experiment on the reaction of water with $dGuo^{\bullet+}$ in DNA. In the experiment, hydrophobic alkyl-substituted cytidines and thymidines were incorporated into the duplex, by which they had expected to repel the otherwise tightly bound water molecules in their vicinity and disrupt the hydration of $dGuo^{\bullet+}$. The experiment did

not produce noticeable changes. Later, they found that a counter ion located in the DNA major groove in proximity to the GG segment could assist the addition of water to ionized DNA.[88]

We were able to detect H-elimination products in the reaction of $9HG^{\bullet+} + D_2O$, which we tend to attribute to a C8-adduct-mediated reaction on the basis of the PES calculation in Fig. 6. The PES is presented for all-H species to allow comparison with the literature (and the differences in reaction enthalpies for deuterated species are less than 0.01 eV). Under single ion-molecule collision conditions, the HE reaction corresponds to $9HG^{\bullet+} + H_2O \rightarrow 9HG^{\bullet+}\cdot W \rightarrow$ TS1·W (C8-water addition) $\rightarrow$ [8-OH-9HG + H]$^{\bullet+}$ (formation of C8-hydroxylated intermediate) $\rightarrow$ TS2 (H elimination) $\rightarrow$ 8-OH-9HG$^+$ + H. $9HG^{\bullet+}\cdot W$ can be characterized as reactants-like with an intermolecular distance of 2.9 Å. The complex is electrostatically bonded, and it is unlikely that there would be activation barrier to its formation. The rate-limiting steps correspond to two tighter activation barriers TS1·W and TS2 with the maximum barrier height being 1.42 eV above reactants. There is another charge state for the HE products, *i.e.* 8-OH-G$^{\bullet}$ + H^+, for which the reaction enthalpy is 9.53 eV and thus was not considered further.

The calculated HE endothermicity is consistent with our experimental observation that the HE cross section increases at high E_{col}. The fact that HE is minor even at high energies could be partially contributed to inter-product channel competition, and partially to the suppression by angular momentum conservation.[89] The reduced mass for HE products is 20 times lower than that for H/D exchange, thus for a given recoil angular momentum, the centrifugal barrier will be roughly an order of magnitude larger. In other words, it was more difficult for the HE products to escape over the centrifugal barrier than for the H/D products. Because H/D exchange itself is a minor channel at high E_{col}, a factor of 20 suppression would shut down HE for $9MG^{\bullet+}$, $dGuo^{\bullet+}$ and $Guo^{\bullet+}$.

Our PES for single-water addition to the C8 of $9HG^{\bullet+}$ agrees with the repulsive reactant interaction reported by Reynisson and Steenken;[27] however, we have identified a non-repulsive reaction route when two water molecules are added to the reaction. As shown by the blue lines in Fig. 6, the second water significantly lowers TS1 for C8-water addition (by 1.4 eV) and there is no barrier for water nucleophilic

addition. Videos for the IRC trajectories crossing TS1·W and TS1·2W are available in the Supporting Information, giving intuitive pictures of single- and double-water reactions with $9HG^{\bullet+}$. TS1·2W features an activation structure where a bond between C8 and a water O atom forms concurrently with the transfer of a water proton towards a neighboring water molecule, and the latter water then transfers a proton to N7. The ″second water-assisted C8-water addition″ is reminiscent of the counter ion-assisted water addition reported by Schuster and co-worker.[88] In both cases, activation barrier diminishes for a reaction that starts from a configuration where a proton (in our experiment) or a Na^+ (in Schuster *et al* ′s) resides at or near the N7 of guanine radical cation and evolves through a TS incorporating a proton shuttle mechanism. The formation of $9HG^{\bullet+}$·2W and TS1·2W provides an explanation for the HE cross section observed at the lowest E_{col} (Fig. 3c), where the combination of long collision time and high D_2O pressure made multiple collisions (up to 8%) and thus three-body reactions possible.

Lastly, we have computed two pathways leading from $[8\text{-OH-}9HG + H]^{\bullet+}$ to $8O\text{-}9HG^{\bullet+}$: one is consecutive elimination of two H atoms. *i.e.* $[8\text{-OH-}9HG + H]^{\bullet+} \rightarrow TS2 \rightarrow 8\text{-OH-}9HG^{+} + H \rightarrow 8O\text{-}9HG^{\bullet+} + 2H$, and the other is concerted H_2 elimination from C8-H and C8-OH, *i.e.* $[8\text{-OH-}9HG + H]^{\bullet+} \rightarrow TS3 \rightarrow 8O\text{-}9HG^{\bullet+} + H_2$. Both pathways require high activation energy (>3 eV) and thus are not feasible in the experiment. We have explored the possibility of forming an enol isomer of $8O\text{-}9HG^{\bullet+}$ (0.47 eV higher in energy than keto) via H_2 elimination from N7-H and C8-H of $[8\text{-OH-}9HG + H]^{\bullet+}$; however, no TS could be located. Alternatively, the enol-isomer could be interconverted directly from $8O\text{-}9HG^{\bullet+}$, and the accompanying transition state is 2.29 eV above $8O\text{-}9HG^{\bullet+}$.

3. The Effects of N9-substitution

$9HG^{\bullet+}$, $9MG^{\bullet+}$, $dGuo^{\bullet+}$ and $Guo^{\bullet+}$ have similar reaction enthalpies and activation barriers. On the basis of the DFT-predicted hydrogen-bonding structures in Fig. 2, one may image that $dGuo^{\bullet+}$ and $Guo^{\bullet+}$ would offer the deoxyribose/ribose OH groups for additional hydrogen bonding such as W3′ and W85′, and form more water complexes. The striking observation is that $9HG^{\bullet+}$ seems the most hydrophilic, while all of the N9-substituents inhibit both complex formation and H/D exchange at low energies. The

fact that the low-E_{col} cross sections of $9MG^{\bullet+}$, $dGuo^{\bullet+}$ and $Guo^{\bullet+}$ are comparable to each other but much lower than that of $9HG^{\bullet+}$ implies that the hydroxyl groups of deoxyribose and ribose have not participated in hydration, at least not to a significant extent. Related to this observation is that Saigusa and co-workers reported similar mono-hydrated structures of dGuo and Guo, from which they have ruled out the hydration of 2′-OH.[90] The same group reported that the lowest-energy structure of $Guo{\cdot}H_2O$ is analogous to that of $9MG{\cdot}H_2O$.[91]

Since the hydration of sugar moiety has been ruled out in our reactions and the DLPNO-CCSD(T)/ωB97XD calculations have indicated that the methyl, 2′-deoxyribose and ribose groups make little difference on reaction enthalpies and activation barriers. We can therefore use $9HG^{\bullet+} + H_2O$ *vs.* $9MG^{\bullet+} + H_2O$ as model systems to capture the physics of the collisions and to delineate the dynamics influence of N9-substituents. The reaction E_{col}-dependence and the trajectory simulations have confirmed that low energy reactions are complex-mediated, thus the missing of a W9 structure seems to be the most likely reason for the reduced reactivity of N9-substituted radical cations. By comparing reaction cross sections and product branching of $9HG^{\bullet+} + H_2O$ and $9MG^{\bullet+} + H_2O$ at 0.1 eV, we may estimate that $9HG^{\bullet+}{\cdot}W9$ may accounts for ~75% of detected water complexes. On the other hand, the yield of W12a in final products may not be as significant as it has shown in the trajectories (cf Fig. 4c); otherwise we would have expected less decreasing for $9MG^{\bullet+}$, $dGuo^{\bullet+}$ and $Guo^{\bullet+}$. The implication is that, in addition to complex formation, reactions involve dynamics factors such as complex lifetimes and orientation, etc. In addition, the formation of W16 was found to be modest in the trajectories. In light of this result, we restate that keto-enol isomerization is dominated by a direct mechanism, and the contribution of W16-mediated keto-enol isomerization should be modest.

V. Summary

The guided ion-beam scattering experiment, reaction PES calculations and dynamics simulations were carried out to discover the mechanism and dynamics for the water attack on guanine radical cations in the gas phase where the deprotonation of guanine radical cation is blocked. Various N9-substituted

guanine radical cations were examined including $9HG^{\bullet+}$, $9MG^{\bullet+}$, $dGuo^{\bullet+}$ and $Guo^{\bullet+}$, in the order of increasing structural complexity. At low E_{col}, the collisions lead to many short-lived complexes with various hydrogen bonds, of which a W9 structure with water hydrogen-bonded to N9-H acts as an important intermediate. The substitution of N9-H blocks the formation of W9, and no hydration of guanosine sugar hydroxyl groups was observed. A combination of these factors results in decreasing reactivity in the order of $9HG^{\bullet+} > 9MG^{\bullet+} > dGuo^{\bullet+} \approx Guo^{\bullet+}$. At high E_{col}, water-catalyzed keto-enol isomerization dominates that occurs by a direct mechanism, except that for $dGuo^{\bullet+}$ and $Guo^{\bullet+}$ where the relatively long-lived W16 complexes may enhance isomerization. Despite being a minor product channel, the most biologically relevant product ions $8\text{-OH-}9HG^{+}$ (a critical intermediate in the post-ionization conversion of guanine nucleobase into OG) were captured in the reaction of $9HG^{\bullet+}$ with water. It was found that C8-water nucleophilic addition has a high activation barrier in the presence of only a single water molecule, but the barrier vanishes once a second water molecule is added to the reaction as a catalyst. It would be interesting to explore the effects of adding more water molecules to the reaction system. Understanding the dynamics of a multiply-hydrated radical system is more challenging, and thus has more intimate biological relevance since the biological reaction environment presents more complex hydrogen bonding structures. Instead of speculating, we plan to simulate the dynamics of two- and three-water-participating C8-hydroxylation in future work. Two simulation approaches will be utilized: the first is to model the reactions of mono-hydrated $9MG^{\bullet+}\cdot H_2O + H_2O$ and dihydrated $9MG^{\bullet+}\cdot(H_2O)_2 + H_2O$, with specific hydrogen bonds in $9MG^{\bullet+}\cdot H_2O$ and $9MG^{\bullet+}\cdot(H_2O)_2$ reactant ions and one of the water ligands specifically attached to C8-H; and the other is to follow trajectories evolving from TS1·2W that connects reactant and the C8-hydroxylated product, so that more insight can be acquired into the dynamics of the reactions of interest.

Supporting Information

Structures and Cartesian coordinates for $9HG^{\bullet+}(H_2O)_{0\text{-}1}$, $9MG^{\bullet+}(H_2O)_{0\text{-}1}$, $dGuo^{\bullet+}(H_2O)_{0\text{-}1}$ and $Guo^{\bullet+}(H_2O)_{0\text{-}1}$, and for reaction species in Figs. 2, 5 and 6. IRC trajectory videos for TS1·W and TS1·2W.

Acknowledgment

This work was supported by the National Science Foundation (Grant No. CHE 1464171), CUNY PSC-CUNY Award and Queens College Research Enhancement Award.

References

1 S. Steenken and S. V. Jovanovic, *J. Am. Chem. Soc.*, 1997, **119**, 617-618.
2 C. J. Burrows and J. G. Muller, *Chem. Rev.*, 1998, **98**, 1109-1151.
3 J. Zhou, O. Kostko, C. Nicolas, X. Tang, L. Belau, M. S. de Vries and M. Ahmed, *J. Phys. Chem. A*, 2009, **113**, 4829-4832.
4 M. Schwell and M. Hochlaf, *Top. Curr. Chem.*, 2015, **355**, 155-208.
5 L. P. Candeias and S. Steenken, *J. Am. Chem. Soc.*, 1989, **111**, 1094-1099.
6 S. Steenken, *Chem. Rev.*, 1989, **89**, 503-520.
7 L. P. Candeias and S. Steenken, *J. Am. Chem. Soc.*, 1992, **114**, 699-704.
8 D. N. Nikogosyan, *Int. J. Radiat. Biol.*, 1990, **57**, 233-299.
9 I. Saito, T. Nakamura and K. Nakatani, *J. Am. Chem. Soc.*, 2000, **122**, 3001-3006.
10 E. D. A. Stemp and J. K. Barton, *Met. Ions Biol. Syst.*, 1996, **33**, 325-365.
11 H. H. Thorp, *Trends Biotechnol.*, 1998, **16**, 117-121.
12 C. Ribaut, G. Bordeau, P. Perio, K. Reybier, V. Sartor, O. Reynes, P.-L. Fabre and N. Chouini-Lalanne, *J. Phys. Chem. B*, 2014, **118**, 2360-2365.
13 H. Kasai, Z. Yamaizumi, M. Berger and J. Cadet, *J. Am. Chem. Soc.*, 1992, **114**, 9692-9694.
14 J. P. Hall, F. E. Poynton, P. M. Keane, S. P. Gurung, J. A. Brazier, D. J. Cardin, G. Winter, T. Gunnlaugsson, I. V. Sazanovich, M. Towrie, C. J. Cardin, J. M. Kelly and S. J. Quinn, *Nat. Chem.*, 2015, **7**, 961-967.
15 T. Caruso, M. Carotenuto, E. Vasca and A. Peluso, *J. Am. Chem. Soc.*, 2005, **127**, 15040-15041.
16 C. E. Crespo-Hernández, D. M. Close, L. Gorb and J. Leszczynski, *J. Phys. Chem. B*, 2007, **111**, 5386-5395.
17 F. D. Lewis, X. Liu, J. Liu, S. E. Miller, R. T. Hayes and M. R. Wasielewski, *Nature*, 2000, **406**, 51-53.
18 J. Cadet, M. Berger, G. W. Buchko, P. C. Joshi, S. Raoul and J.-L. Ravanat, *J. Am. Chem. Soc.*, 1994, **116**, 7403-7404.
19 L. P. Candeias and S. Steenken, *Chem. - Eur. J.*, 2000, **6**, 475-484.
20 J. Cadet, T. Douki and J.-L. Ravanat, *Acc. Chem. Res.*, 2008, **41**, 1075-1083.
21 W. L. Neeley and J. M. Essigmann, *Chem. Res. Toxicol.*, 2006, **19**, 491-505.
22 O. R. Alshykhly, A. M. Fleming and C. J. Burrows, *J. Org. Chem.*, 2015, **80**, 6996-7007.
23 A. M. Fleming and C. J. Burrows, *Free Radic. Biol. Med.*, 2017, **107**, 35-52.
24 A. Adhikary, A. Kumar, D. Becker and M. D. Sevilla, *J. Phys. Chem. B*, 2006, **110**, 24171-24180.
25 K. Kobayashi and S. Tagawa, *J. Am. Chem. Soc.*, 2003, **125**, 10213-10218.
26 K. Kobayashi, R. Yamagami and S. Tagawa, *J. Phys. Chem. B*, 2008, **112**, 10752-10757.
27 J. Reynisson and S. Steenken, *Phys. Chem. Chem. Phys.*, 2002, **4**, 527-532.
28 Y. Rokhlenko, N. E. Geacintov and V. Shafirovich, *J. Am. Chem. Soc.*, 2012, **134**, 4955-4962.
29 Y. Rokhlenko, J. Cadet, N. E. Geacintov and V. Shafirovich, *J. Am. Chem. Soc.*, 2014, **136**, 5956-5962.
30 K. Hildenbrand and D. Schulte-Frohlinde, *Free Radical Res. Commun.*, 1990, **11**, 195-206.
31 S. D. Wetmore, R. J. Boyd and L. A. Eriksson, *J. Phys. Chem. B*, 1998, **102**, 9332-9343.
32 H. Sies, *Oxidative Stress*, Academic Press, 1985.
33 S. Boiteux and J. P. Radicella, *Biochimie*, 1999, **81**, 59-67.
34 B. Armitage, *Chem. Rev.*, 1998, **98**, 1171-1200.
35 S. D. Bruner, D. P. G. Norman and G. L. Verdine, *Nature*, 2000, **403**, 859-866.

36 M. A. Lovell and W. R. Markesbery, *Arch. Neurol.*, 2001, **58**, 392-396.
37 J. Zhang, G. Perry, M. A. Smith, D. Robertson, S. J. Olson, D. G. Graham and T. J. Montine, *Am. J. Pathol.*, 1999, **154**, 1423-1429.
38 X. Xu, J. G. Muller, Y. Ye and C. J. Burrows, *J. Am. Chem. Soc.*, 2008, **130**, 703-709.
39 T. Douki, S. Spinelli, J.-L. Ravanat and J. Cadet, *J. Chem. Soc., Perkin Trans. 2*, 1999, 1875-1880.
40 B. Giese and M. Spichty, *ChemPhysChem*, 2000, **1**, 195-198.
41 J. A. Dean, *Lange's Handbook of Chemistry, Fifteenth Edition*, McGraw-Hill, New York, 1999.
42 L. Wu, K. Liu, J. Jie, D. Song and H. Su, *J. Am. Chem. Soc.*, 2015, **137**, 259-266.
43 J. Choi, C. Yang, M. Fujitsuka, S. Tojo, H. Ihee and T. Majima, *J. Phys. Chem. Lett.*, 2015, **6**, 5045-5050.
44 A. W. Parker, C. Y. Lin, M. W. George, M. Towrie and M. K. Kuimova, *J. Phys. Chem. B*, 2010, **114**, 3660-3667.
45 T. J. Merta, N. E. Geacintov and V. Shafirovich, *Photochem. Photobiol.*, 2018, DOI: 10.1111/php.12926.
46 Y. Yang, H. Su, W. Fang, X. Chen and W. Yang, *Phys Chem Chem Phys*, 2018, **20**, 13598-13606.
47 J. M. Rice and G. O. Dudek, *J. Amer. Chem. Soc.*, 1967, **89**, 2719-2725.
48 A. Liguori, A. Napoli and G. Sindona, *J. Am. Soc. Mass Spectrom.*, 2001, **12**, 176-179.
49 I. K. Chu, C. F. Rodriquez, T.-C. Lau, A. C. Hopkinson and K. W. M. Siu, *J. Phys. Chem. B*, 2000, **104**, 3393-3397.
50 S. Wee, R. A. J. O'Hair and W. D. McFadyen, *Rapid Commun. Mass Spectrom.*, 2005, **19**, 1797-1805.
51 A. K. Y. Lam, B. F. Abrahams, M. J. Grannas, W. D. McFadyen and R. A. J. O'Hair, *Dalton Trans.*, 2006, 5051-5061.
52 P. Cheng and D. K. Bohme, *J. Phys. Chem. B*, 2007, **111**, 11075-11082.
53 L. Feketeová, E. Yuriev, J. D. Orbell, G. N. Khairallah and R. A. J. O'Hair, *Int. J. Mass Spectrom.*, 2011, **304**, 74-82.
54 Y. Fang and J. Liu, *J. Phys. Chem. A*, 2009, **113**, 11250-11261.
55 L. Feketeová, B. Chan, G. N. Khairallah, V. Steinmetz, P. Maître, L. Radom and R. A. J. O'Hair, *Phys. Chem. Chem. Phys.*, 2015, **17**, 25837-25844.
56 N. Agnihotri and P. C. Mishra, *J. Phys. Chem. B*, 2009, **113**, 3129-3138.
57 A. Yadav and P. C. Mishra, *Int. J. Quantum Chem.*, 2012, **112**, 2000-2008.
58 A. Kumar and M. D. Sevilla, *J. Phys. Chem. B*, 2014, **118**, 5453-5458.
59 B. T. Psciuk and H. B. Schlegel, *J. Phys. Chem. B*, 2013, **117**, 9518-9531.
60 J.-D. Chai and M. Head-Gordon, *Phys. Chem. Chem. Phys.*, 2008, **10**, 6615-6620.
61 E. Caueet, D. Dehareng and J. Lievin, *J. Phys. Chem. A*, 2006, **110**, 9200-9211.
62 D. Roca-Sanjuán, M. Rubio, M. Merchán and L. Serrano-Andrés, *J. Chem. Phys.*, 2006, **125**, 084302.
63 L. Zhang, Y. Pan and F. Qi, *J. Theor. Comput. Chem.*, 2009, **8**, 1103-1115.
64 D. G. Liakos, M. Sparta, M. K. Kesharwani, J. M. L. Martin and F. Neese, *J. Chem. Theory Comput.*, 2015, **11**, 1525-1539.
65 L. Feketeová, G. N. Khairallah, B. Chan, V. Steinmetz, P. Maître, L. Radom and R. A. J. O'Hair, *Chem. Commun.* , 2013, **49**, 7343-7345.
66 I. M. Alecu, J. Zheng, Y. Zhao and D. G. Truhlar, *J. Chem. Theory Comput.*, 2010, **6**, 2872-2887.
67 M. J. Frisch, G. W. Trucks, H. B. Schlegel, G. E. Scuseria, M. A. Robb, J. R. Cheeseman, G. Scalmani, V. Barone, B. Mennucci, G. A. Petersson, H. Nakatsuji, M. Caricato, X. Li, H. P. Hratchian, A. F. Izmaylov, J. Bloino, G. Zheng, J. L. Sonnenberg, M. Hada, M. Ehara, K. Toyota, R. Fukuda, J. Hasegawa, M. Ishida, T. Nakajima, Y. Honda, O. Kitao, H. Nakai, T. Vreven, J. J. A. Montgomery, J. E. Peralta, F. Ogliaro, M. Bearpark, J. J. Heyd, E. Brothers, K. N. Kudin, V. N. Staroverov, T. Keith, R. Kobayashi, J. Normand, K. Raghavachari, A. Rendell, J. C. Burant, S. S. Iyengar, J. Tomasi, M. Cossi, N. Rega, J. M. Millam, M. Klene, J. E. Knox, J. B. Cross, V. Bakken, C. Adamo, J. Jaramillo, R. Gomperts, R. E. Stratmann, O. Yazyev, A. J. Austin, R. Cammi, C. Pomelli, J. W. Ochterski, R. L. Martin, K. Morokuma, V. G. Zakrzewski, G. A. Voth, P. Salvador, J. J. Dannenberg, S. Dapprich, A. D. Daniels, O. Farkas, J. B.

Foresman, J. V. Ortiz, J. Cioslowski and D. J. Fox, Gaussian 09, Revision D.01, Gaussian, Inc, Wallingford, CT, 2013.

68 F. Neese, *Wiley Interdiscip. Rev.: Comput. Mol. Sci.*, 2012, **2**, 73-78.

69 R. A. Marcus, *J. Chem. Phys.*, 1952, **20**, 359-364.

70 L. Zhu and W. L. Hase, A general RRKM program (QCPE 644), Quantum chemistry program exchange, Chemistry Department, University of Indiana, Bloomington, 1993.

71 X. Hu, W. L. Hase and T. Pirraglia, *J. Comput. Chem.*, 1991, **12**, 1014-1024.

72 W. L. Hase, K. Bolton, P. de Sainte Claire, R. J. Duchovic, X. Hu, A. Komornicki, G. Li, K. Lim, D. Lu, G. H. Peslherbe, K. Song, K. N. Swamy, S. R. Vande Linde, A. Varandas, H. Wang and R. J. Wolf, VENUS 99: A general chemical dynamics computer program, Texas Tech Univeristy Lubbock, TX, 1999.

73 V. Bakken, J. M. Millam and H. B. Schlegel, *J. Chem. Phys.*, 1999, **111**, 8773-8777.

74 G. H. Peslherbe, H. Wang and W. L. Hase, *Adv. Chem. Phys.*, 1999, **105**, 171-201.

75 L. Laaksonen, gOpenMol, Center for Scientific Computing, Espoo, Finland, 3.0 edn., 2005, available at www.csc.fi/gopenmol/.

76 T. J. Lee and P. R. Taylor, *Int. J. Quantum Chem., Quantum Chem. Symp.*, 1989, **36**, 199-207.

77 E. Nir, I. Huenig, K. Kleinermanns and M. S. de Vries, *ChemPhysChem*, 2004, **5**, 131-137.

78 H. Asami, S.-h. Urashima, M. Tsukamoto, A. Motoda, Y. Hayakawa and H. Saigusa, *J. Phys. Chem. Lett.*, 2012, **3**, 571-575.

79 H. Saigusa, N. Mizuno, H. Asami, K. Takahashi and M. Tachikawa, *Bull. Chem. Soc. Jpn.*, 2008, **81**, 1274-1281.

80 J. Troe, *Chem. Phys. Lett.*, 1985, **122**, 425-430.

81 W. L. Hase ed., *Advances in classical trajectory methods, Vol. 1: Intramolecular and nonlinear dynamics*, JAI, Greenwich, 1998.

82 M. Döntgen, M.-D. Przybylski-Freund, L. C. Kröger, W. A. Kopp, A. E. Ismail and K. Leonhard, *J. Chem. Theory Comput.*, 2015, **11**, 2517-2524.

83 E. Martínez-Núñez, *Phys. Chem. Chem. Phys.*, 2015, **17**, 14912-14921.

84 S. Pratihar, X. Ma, Z. Homayoon, G. L. Barnes and W. L. Hase, *J. Am. Chem. Soc.*, 2017, **139**, 3570-3590.

85 M. T. Rodgers, K. M. Ervin and P. B. Armentrout, *J. Chem. Phys.*, 1997, **106**, 4499-4508.

86 P. Liu, C. Li, S. Wang and D. Wang, *J. Phys. Chem. B*, 2018, **122**, 3124-3132.

87 F. O. Onyemauwa and G. B. Schuster, *Photochem. Photobiol.*, 2006, **82**, 729-732.

88 R. N. Barnett, A. Bongiorno, C. L. Cleveland, A. Joy, U. Landman and G. B. Schuster, *J. Am. Chem. Soc.*, 2006, **128**, 10795-10800.

89 H.-T. Kim, J. Liu and S. L. Anderson, *J. Chem. Phys.*, 2001, **115**, 1274-1286.

90 H. Asami, S.-H. Urashima and H. Saigusa, *Phys. Chem. Chem. Phys.*, 2009, **11**, 10466-10472.

91 H. Saigusa, S.-h. Urashima and H. Asami, *J. Phys. Chem. A*, 2009, **113**, 3455-3462

Scheme 1 Chemical transformations of guanine radical cation.

Abbreviations: FapyG, 2,6-diamino-4-hydroxy-5-formamidopyrimidine; 2Ih, 5-carboxamido-5-formamido-2-iminohydantoin; Iz, 2,5-diaminoimidazolone; OG, 8-oxo-7,8-dihydroguanine; 8-OH-G•, 8-hydroxylated guanine radical; Sp, spiroiminodihydantoin; Z, 2,2,4-triamino-2H-oxazol-5-one.

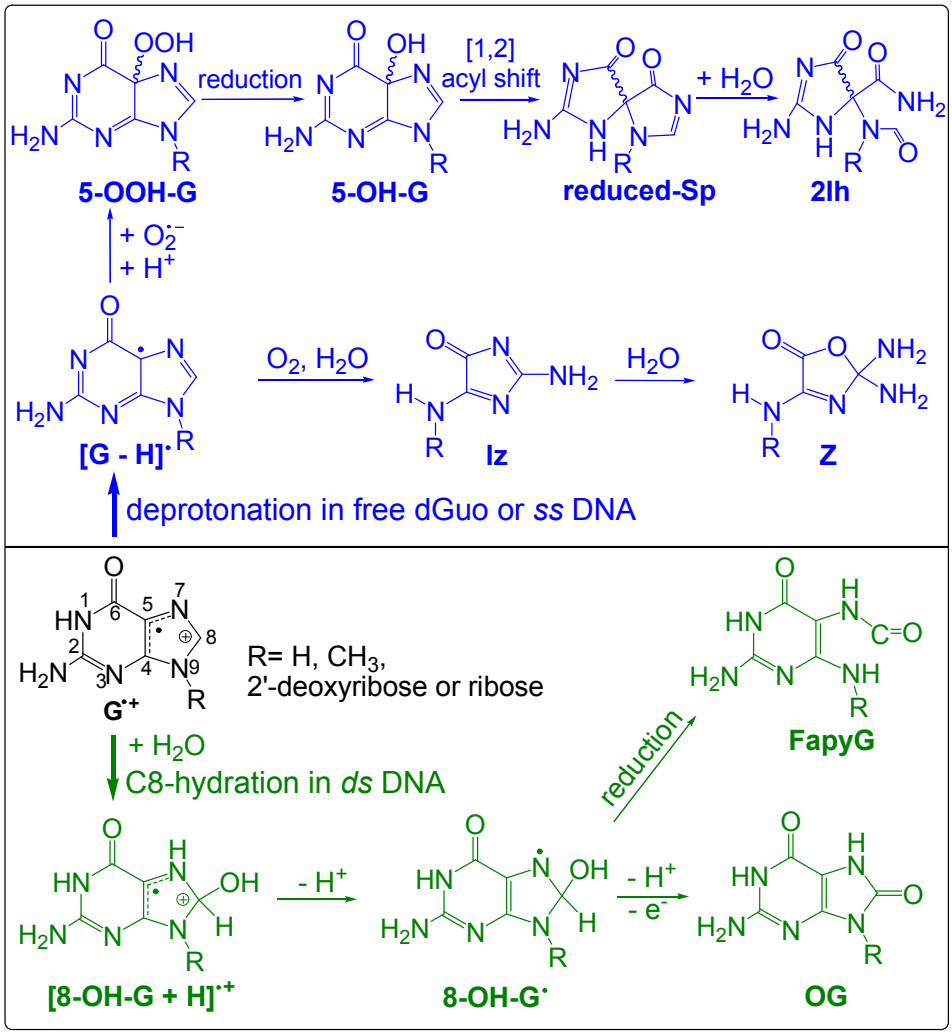

Figure Captions

Fig. 1 Lowest-lying keto and enol conformers of $9HG^{\bullet+}$, $9MG^{\bullet+}$, $dGuo^{\bullet+}$ and $Guo^{\bullet+}$. Atomic numbering schemes are presented. Spin (contour plots) and charge densities (numbers) were calculated at ωB97XD/6-31+G(d,p). Energies (eV) of enols *vs*. ketos were evaluated at DLPNO-CCSD(T)/aug-cc-pVTZ//ωB97XD/6-31+ G(d,p) with 298 K thermal corrections.

Fig. 2 Mono-hydrates of $9HG^{\bullet+}$, $9MG^{\bullet+}$, $dGuo^{\bullet+}$ and $Guo^{\bullet+}$. Atom numbering scheme and nomenclature are presented. Hydration sites are indicated by the last two numbers in notations, and hydrogen bonds are depicted by dashed lines with lengths shown in Å. Relative energies (eV, with respect to global minima) and hydration enthalpies were evaluated for all-H systems at DLPNO-CCSD(T)/aug-cc-pVTZ//ωB97XD/6-31+ G(d,p) with 298 K thermal corrections. A D_2O ligand increases hydration enthalpy by ≤ 0.01 eV.

Fig. 3 Product cross sections for the reactions of D_2O with $9HG^{\bullet+}$, $9MG^{\bullet+}$, $dGuo^{\bullet+}$ and $Guo^{\bullet+}$ as a function of center-of-mass collision energy.

Fig. 4 a, b) Representative complex-forming trajectories for $9MG^{\bullet+} + H_2O$, simulated at $E_{col} = 0.1$ eV. Each set shows the changes of PE and the CM separation between collision partners (right axis), and the formation of hydrogen bonds; and c) formation probabilities of different complex structures in the trajectories of $9HG^{\bullet+}$ + water and $9MG^{\bullet+}$ + water. Distribution probabilities are based on 100 trajectories for each system.

Fig. 5 PES for keto-enol isomerization of $9HG^{\bullet+}$ in the presence and the absence of water. Reaction enthalpies (eV, for all-H species) were determined on the basis of electronic energies at DLPNO-CCSD(T)/aug-cc-pVTZ//ωB97XD/6-31+G(d,p), and 298 K thermal corrections at ωB97XD/ 6-31+G(d,p). For TSs, vibrational modes corresponding to imaginary frequencies are indicated by displacement vectors. Numbers in parentheses are reaction enthalpies with D_2O.

Fig. 6 PES for C8-water addition to $9HG^{\bullet+}$. Reaction enthalpies (eV, for all-H species) were determined by the sum of electronic energies calculated at DLPNO-CCSD(T)/aug-cc-pVTZ //ωB97XD/6-31+G(d,p), and 298 K thermal corrections at ωB97XD/6-31+G(d,p). Structures of TS2·W and 8-OH-$9HG^{+}$·W are similar to their dry analogous except a water bonded to N7-H and C6-O. Trajectories (in MP4 format) for $9HG^{\bullet+} + H_2O \rightarrow$ TS1·W $\rightarrow$ $[8\text{-OH-9HG} + H]^{\bullet+}$ and $9HG^{\bullet+} + 2H_2O \rightarrow$ TS1·2W $\rightarrow$ $[8\text{-OH-9HG} + H]^{\bullet+} + H_2O$ are available in the Supporting Information.

Fig. 1

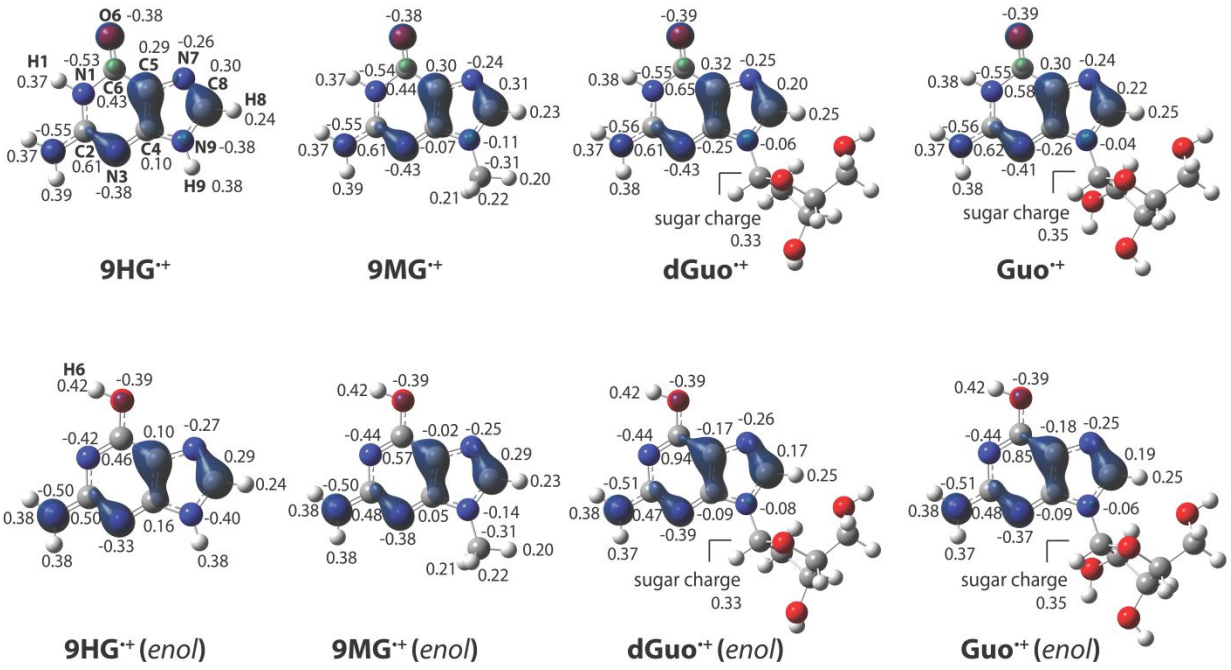
9HG•+
9MG•+
dGuo•+
Guo•+
sugar charge
0.33
sugar charge
0.35
9HG•+ (enol)
9MG•+ (enol)
dGuo•+ (enol)
Guo•+ (enol)
sugar charge
0.33
sugar charge
0.35

Fig. 2

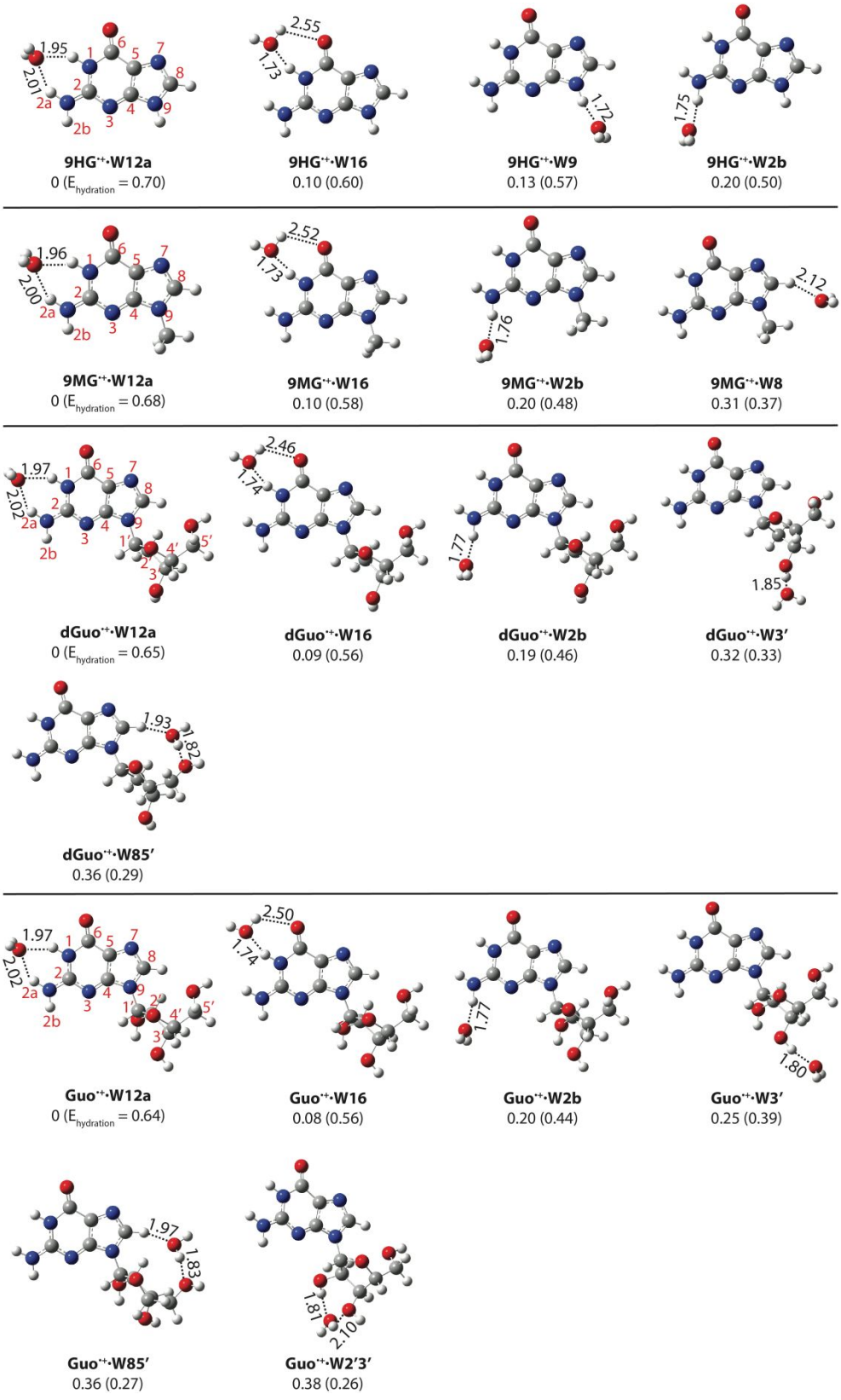
9HG•+·W12a
0 (E hydration = 0.70)
9HG•+·W16
0.10 (0.60)
9HG•+·W9
0.13 (0.57)
9HG•+·W2b
0.20 (0.50)
9MG•+·W12a
0 (E hydration = 0.68)
9MG•+·W16
0.10 (0.58)
9MG•+·W2b
0.20 (0.48)
9MG•+·W8
0.31 (0.37)
dGuo•+·W12a
0 (E hydration = 0.65)
dGuo•+·W16
0.09 (0.56)
dGuo•+·W2b
0.19 (0.46)
dGuo•+·W3′
0.32 (0.33)
dGuo•+·W85′
0.36 (0.29)
Guo•+·W12a
0 (E hydration = 0.64)
Guo•+·W16
0.08 (0.56)
Guo•+·W2b
0.20 (0.44)
Guo•+·W3′
0.25 (0.39)
Guo•+·W85′
0.36 (0.27)
Guo•+·W2′3′
0.38 (0.26)

Fig. 3

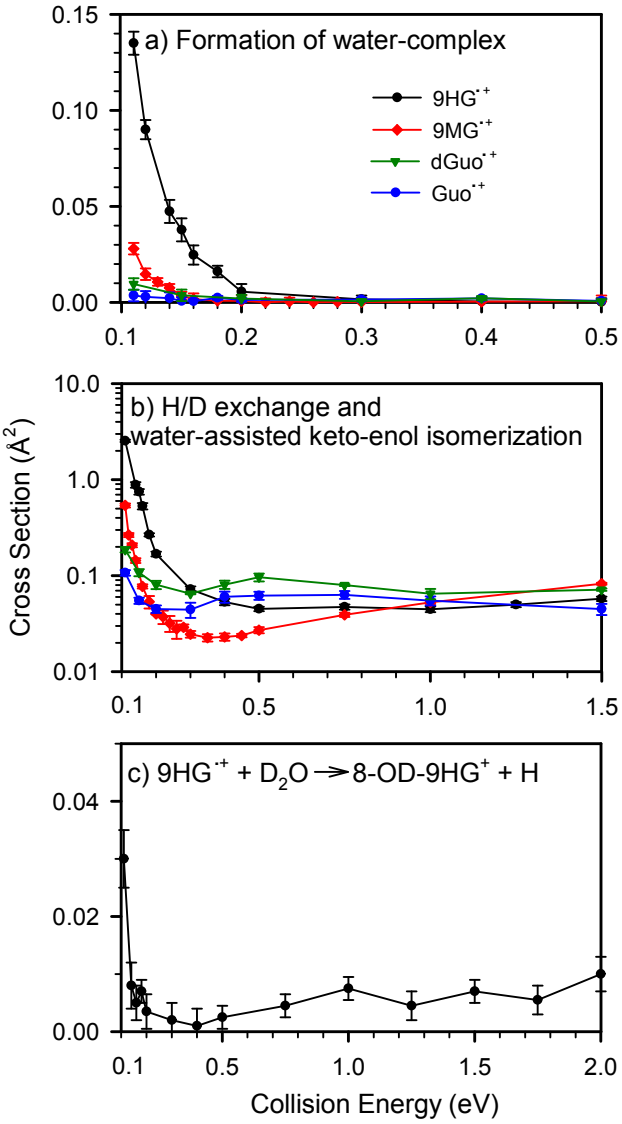
a) Formation of water-complex
9HG•+
9MG•+
dGuo•+
Guo•+
b) H/D exchange and
water-assisted keto-enol isomerization
c) 9HG•+ + D2O → 8-OD-9HG+ + H
Cross Section (Å2)
Collision Energy (eV)

Fig. 4

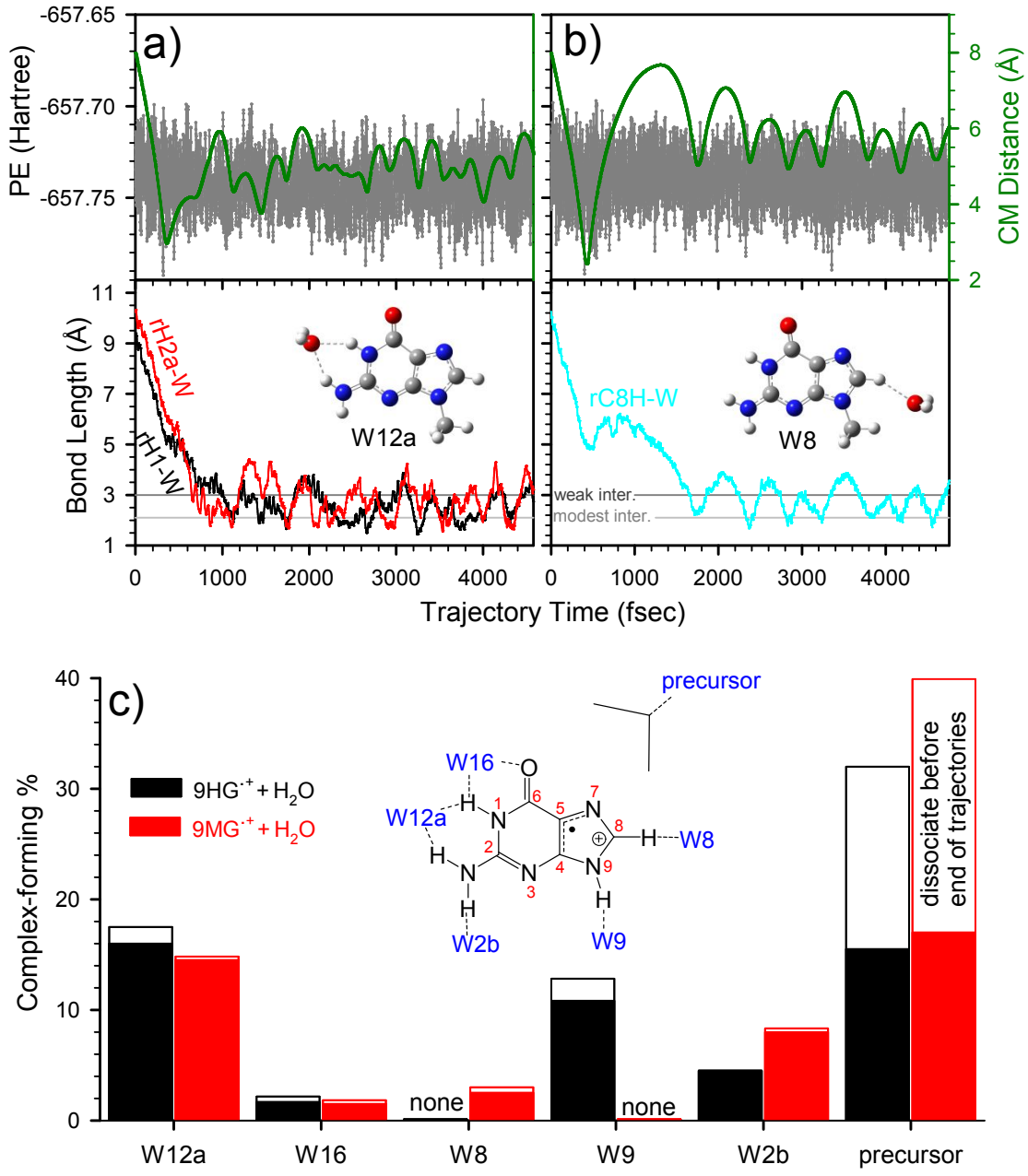
a)
b)
PE (Hartree)
-657.65
-657.70
-657.75
CM Distance (Å)
Bond Length (Å)
rH2a-W
rH1-W
rC8H-W
W12a
W8
weak inter.
modest inter.
Trajectory Time (fsec)
c)
Complex-forming %
9HG·+ + H2O
9MG·+ + H2O
precursor
W16
W12a
W8
W2b
W9
dissociate before end of trajectories
none
none
W12a
W16
W8
W9
W2b
precursor

Fig. 5

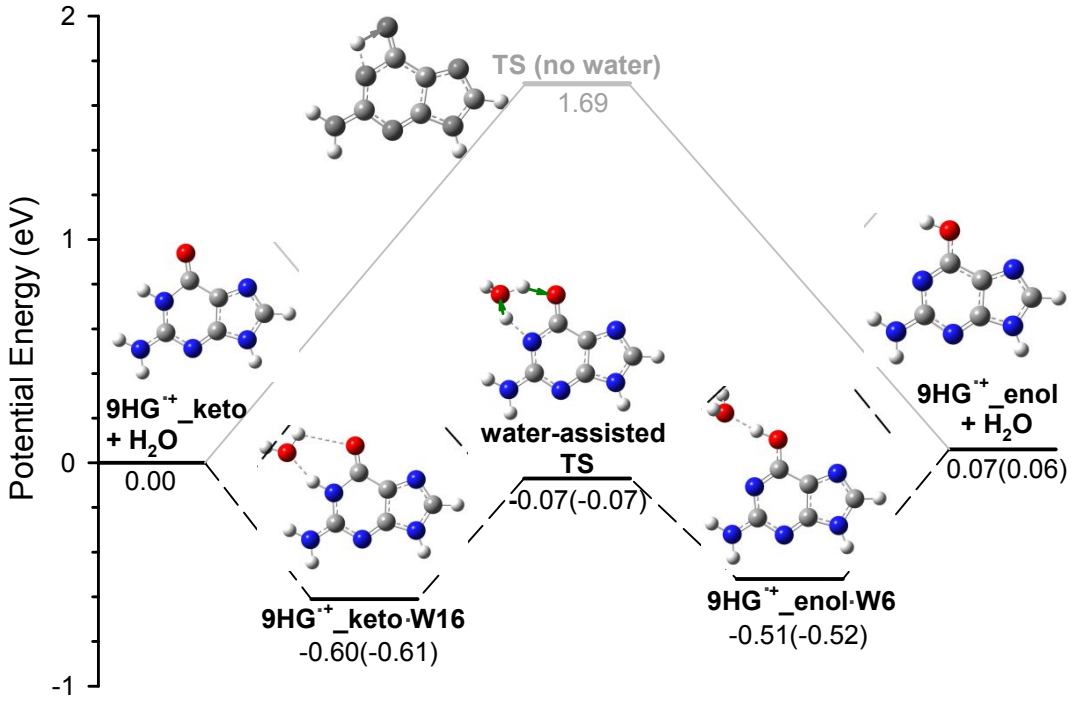
Potential Energy (eV)
2
1
0
-1
TS (no water)
1.69
9HG•+_keto
+ H2O
0.00
9HG•+_keto·W16
-0.60(-0.61)
water-assisted
TS
-0.07(-0.07)
9HG•+_enol·W6
-0.51(-0.52)
9HG•+_enol
+ H2O
0.07(0.06)

Fig. 6

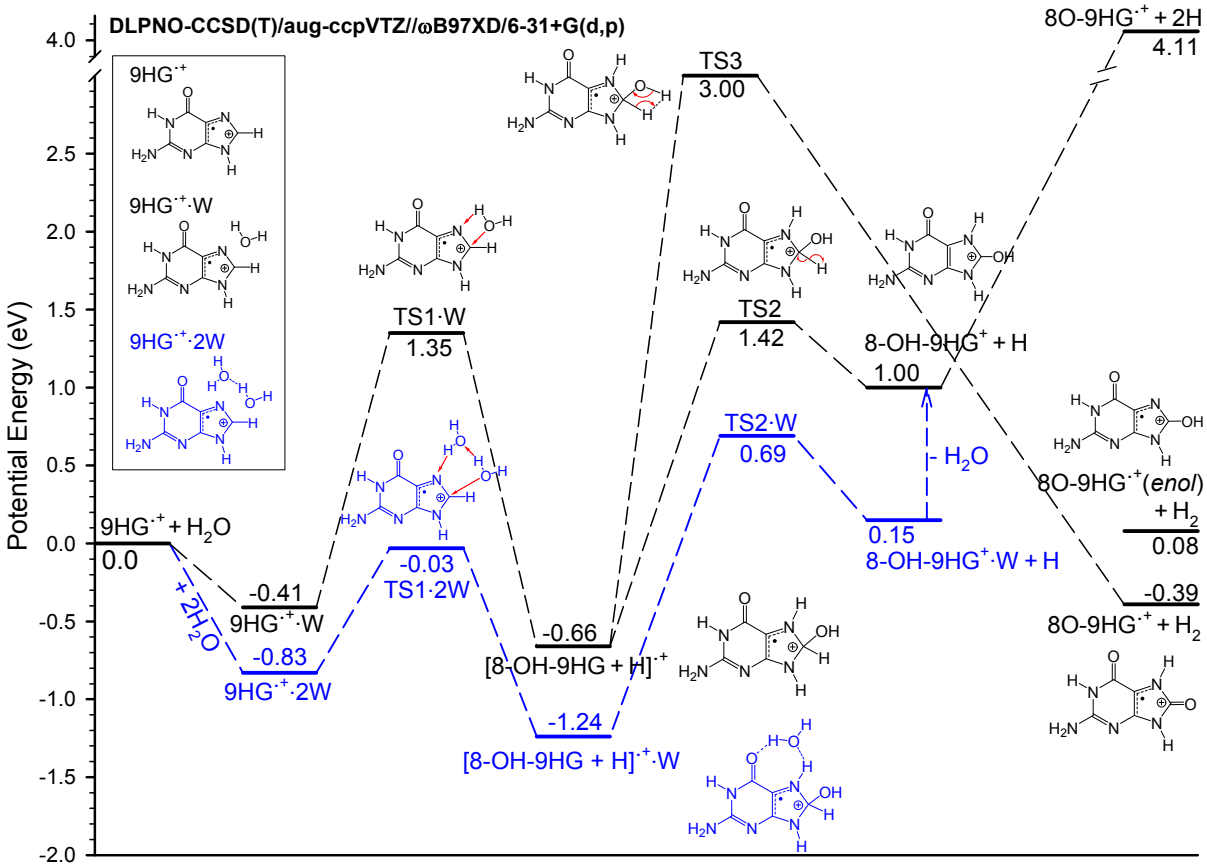
DLPNO-CCSD(T)/aug-ccpVTZ//ωB97XD/6-31+G(d,p)
Potential Energy (eV)
9HG·+
9HG·+·W
9HG·+·2W
9HG·+ + H2O
0.0
-0.41
9HG·+·W
-0.83
9HG·+·2W
+ 2H2O
TS1·W
1.35
-0.03
TS1·2W
-0.66
[8-OH-9HG + H]·+
-1.24
[8-OH-9HG + H]·+·W
TS3
3.00
TS2
1.42
TS2·W
0.69
8-OH-9HG+ + H
1.00
- H2O
0.15
8-OH-9HG+·W + H
8O-9HG·+ + 2H
4.11
8O-9HG·+(enol)
+ H2
0.08
-0.39
8O-9HG·+ + H2

TOC

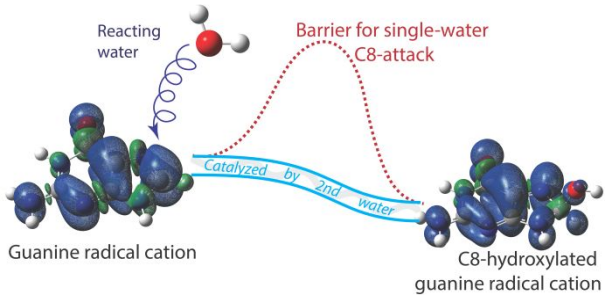
Reacting water
Barrier for single-water C8-attack
Catalyzed by 2nd water
Guanine radical cation
C8-hydroxylated guanine radical cation